GSA Data Repository 2012063

Splay fault slip during the M_w 8.8 2010 Maule Chile earthquake

Daniel Melnick, Marcos Moreno, Mahdi Motagh, Marco Cisternas, Robert L. Wesson

Estimating coseismic coastal uplift at Isla Santa María

We estimated coastal uplift associated with the Maule earthquake at 10 sites using: (1) the post-earthquake elevation of the sessile mussel *Perumytilus purpuratus* attached to rocks relative to their normal growth levels (Melnick et al., 2011); (2) a geodetic benchmark installed by the Hydrographic and Oceanographic Survey of the Chilean Navy (SHOA) at the peer in Puerto Sur; and (3) survey-type Global Positioning System (GPS) measurements (Table DR1).

In 2004, we installed three GPS monuments at Isla Santa María (ISM) in the frame of the SAGA (South American Geodetic Activities) and COGA (Concepción Geodetic Activities) projects (Moreno et al., 2008; Moreno, 2010; Moreno et al., 2011). Two of these sites (STDO and STCA) were surveyed 6 times before and 3 times after the 2010 earthquake. The third site (STMA) was surveyed only twice before and twice after the earthquake. We started to survey the sites 11-13 days after the earthquake. The data was processed following the strategy described in (Moreno et al., 2008; Moreno, 2010; Moreno et al., 2011) using the Bernese v5.0 software. Unfortunately, a large landslide occurred at the sea cliff adjacent to site STCA and concave cracks from the headscarp extended within 50 cm from the monument. Though the coseismic horizontal displacement agrees well with those obtained at the other two sites, the magnitude of uplift is 29 to 43 cm lower. We cannot reject the local effect of mass wasting and thus we discard this site from our analysis of coastal uplift (Figure 2C).

Synthetic Aperture Radar Interferometry (InSAR)

We used two radar images acquired by the Japanese ALOS satellite in an ascending orbit (Figure DR3 and Table DR2) to estimate coseismic deformation at ISM during the 2010 earthquake. The data have been processed using the SARscape software. We followed a

typical repeat-pass processing procedure and removed the topographic phase contribution to the interferometric phase using a 5-m DEM derived from photogrammetry processing of 1:20,000 scale air photos with GPS ground control points (Melnick et al., 2006). The differential interferogram was then filtered using a weighted power spectrum technique (Goldstein and Werner, 1998), unwrapped using the SNAPHU software (Chen and Zebker, 2001), and mapped from the original SAR system onto a geographic grid using the 5-m DEM.

Interviews with local inhabitants

Surface fault rupture at Isla Santa María (ISM) were discovered by Eucebio Loyola, a 55-year inhabitant of the town of Puerto Norte. He was in his house during the earthquake, which is located at 100 m from the surface ruptures and noticed the fault breaks at dawn, about 2.5 hours after the earthquake's mainshock (03:36 UTC -0300). During this reconnaissance visit, he noticed that fluids were bubbling out of the surface breaks at several locations along the entire ~150-m-long fault. According to him and other inhabitants, fluids continued to bubble intensely for three days after the earthquake, and kept emerging from the fault for weeks.

Maps, descriptions, and field views of coseismic surface ruptures

We mapped the extent of surface ruptures at Isla Santa María (ISM), with the aid of the Leica 1200 GNSS (Global Navigation Satellite System) differential Global Positioning System (dGPS) in kinematic survey mode. To minimize instrumental errors, we used a mobile base station, ensuring base-rover distances of less than 1 km. In addition, we used data from our geodetic GPS station STDO at ISM and from IGS (International GPS System) site CONZ, located at 52 km northeast from ISM, to correct the static data from the local base station. Given the instrumental configuration, good weather conditions during our survey, and excellent satellite visibility provided by an open sky at the flat island, the measurement errors were found to be always below 1 cm. Vertical offsets across the fault were estimated using measuring tape and static GPS positioning. Field photographs and maps from our dGPS survey overlaid on aerial images of the fault ruptures are shown on Figures DR4-DR9.

Active faults at ISM had been first observed during a reconnaissance flight in 2004 (Figure DR5A). Six years before the Maule earthquake, we recognized a NE-striking half-graben consisting of a main NW-dipping primary normal fault and a SE-dipping antithetic

fault. The structures were well exposed on the active sea cliff along the western coast of the island (Figure DR5B). Large landslides triggered by the earthquake covered this region hindering access to the base of the cliff (Figure DR6C). The 2010 surface rupture occurred along the northern, SE-dipping antithetic fault of the half-graben (Figure DR5B).

In map view, surface ruptures can be grouped in three distinct segments (Figure DR4):

1. The western fault segment, consisting of NE-SW oriented, right and left-stepping en échelon fault traces (Figure DR6). Maximum vertical throw is 30 cm near the sea cliff (Figure 3B, Table DR4), decreasing to 15 cm across a paved road (Figure DR6A), and to zero farther to the northeast. This part of the fault had been recognized in 2004 (Melnick et al., 2006) on sea cliff exposures offsetting the ~53-ka-old base of the late Pleistocene marine sediments (Figure DR5B) as well as on a road cut adjacent to the 2010 rupture offsetting ~27-ka-old eolian strata (Figure DR6B). At these two sites, the magnitude of pre-2010 and 2010 displacements is very similar. We found no evidence of a clear strike-slip component.

2. The central transfer zone integrates E-W striking, left-stepping faults with between 5 and 10 cm of vertical throw exposed along a steep valley flank (Figure DR7). To the west, the fault rupture dies on a water spring. No evidence of strike-slip motion was found on this part of the rupture.

3. The eastern fault segment has an overall downslope-convex geometry (Figure DR8) and consists of several left and right-stepping en échelon traces. We measured the maximum vertical throw of 82 cm near the center of this segment (Figure DR8B). Displacement increases bilaterally towards the center of the segment (Figure 3B and Figure DR8A, Table DR4). Fluid offspring occurred continuously during the weeks that followed the earthquake along the easternmost part of this segment (Figure DR8C, DR11).

Volume of coseismic fluid outflow

We estimated the volume of fluid outflow through the surface fault break at ISM by mapping the extent of the Pajonal Lagoon on a pair of aerial photos collected 7 days before and 24 days after the earthquake with the same camera (Figures DR11). These color digital aerial photos have a resolution of ~25 cm, and have been georeferenced using dGPS ground control points. To estimate the volume, we mapped the water body of the lagoon and overlaid them on a 5-m digital elevation model (Figure 3A).

According to eyewitnesses at hand, water rushed and bubbled intensively from the fault break during three days after the earthquake, causing an immediate water level raise of the adjacent lagoon (Figure DR12). We found no debris or sand left by the tsunami in the lagoon; in agreement with the eyewitnesses' reports on the tsunami failing to reach the lagoon. In addition, no evident tsunami deposit or associated erosive marks from tsunami back-flow was observed in the field or on the post-earthquake air photo (Figure DR11B). Thus, the rise of water level was not a result of tsunami inundation. This sudden rise led inhabitants to dig, before our visit, a channel across the outlet sand bar to drain the lake, visible on the right side of the post-earthquake image (Figure DR11B). Thus, the post-earthquake aerial photo was taken with the drained lake and hence the volume estimated has to be considered a minimum of the amount of fluids that rushed through the fault break.

A well-expressed shoreline is observed surrounding the lagoon on the pre-earthquake image (white arrows in Figure DR11A), which corresponds to the overflow level of the lagoon, located at an elevation of between 4.3 and 4.5 m. As a result of fluid offspring from the surface rupture, water reached the overflow level and started to drain towards the ocean along the narrow artificial channel dug by inhabitants (Figure DR11B). The level of the lagoon before the earthquake was at between 3 and 3.2 m, and thus the increase in level associated with the earthquake was between 1.1 and 1.5 m. The area of the lagoon is 15,700 m^2, and therefore a volume of water between 17,270 and 23,550 m^3 accumulated in the lagoon to reach the overflow level. Because this area lacked precipitation in the weeks following the earthquake, this volume can be considered the minimum volume of fluid that rushed to the surface through the fault rupture.

The volume of water accumulated in the lagoon, which is the minimum volume of fluids that rushed from the fault, is similar to the amount of precipitation in the 6 to 7 months previous to the earthquake at ISM (Figure DR13), estimated using the 71,000-m^2 catchment area draining the fault rupture region.

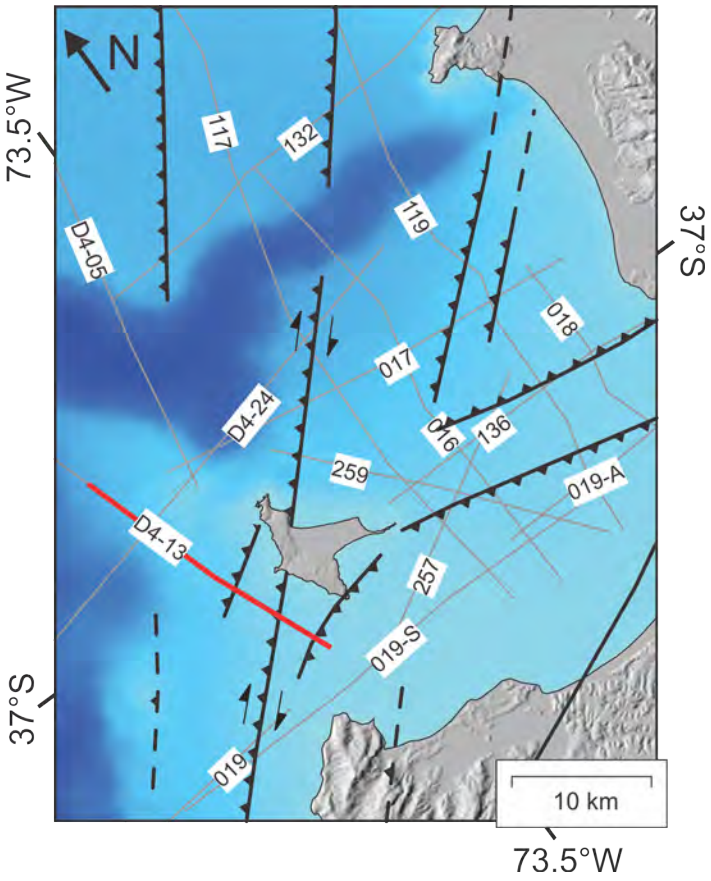

Figure DR1. Map of subsurface blind reverse faults in the Arauco Bay area (same area as Figure 1B) and location of ENAP seismic reflection profiles available for this study. See Figure 1A for location and (Melnick et al., 2006; Melnick and Echtler, 2006; Melnick et al., 2009) for detailed descriptions of the seismic stratigraphy and subsurface structure in this region.

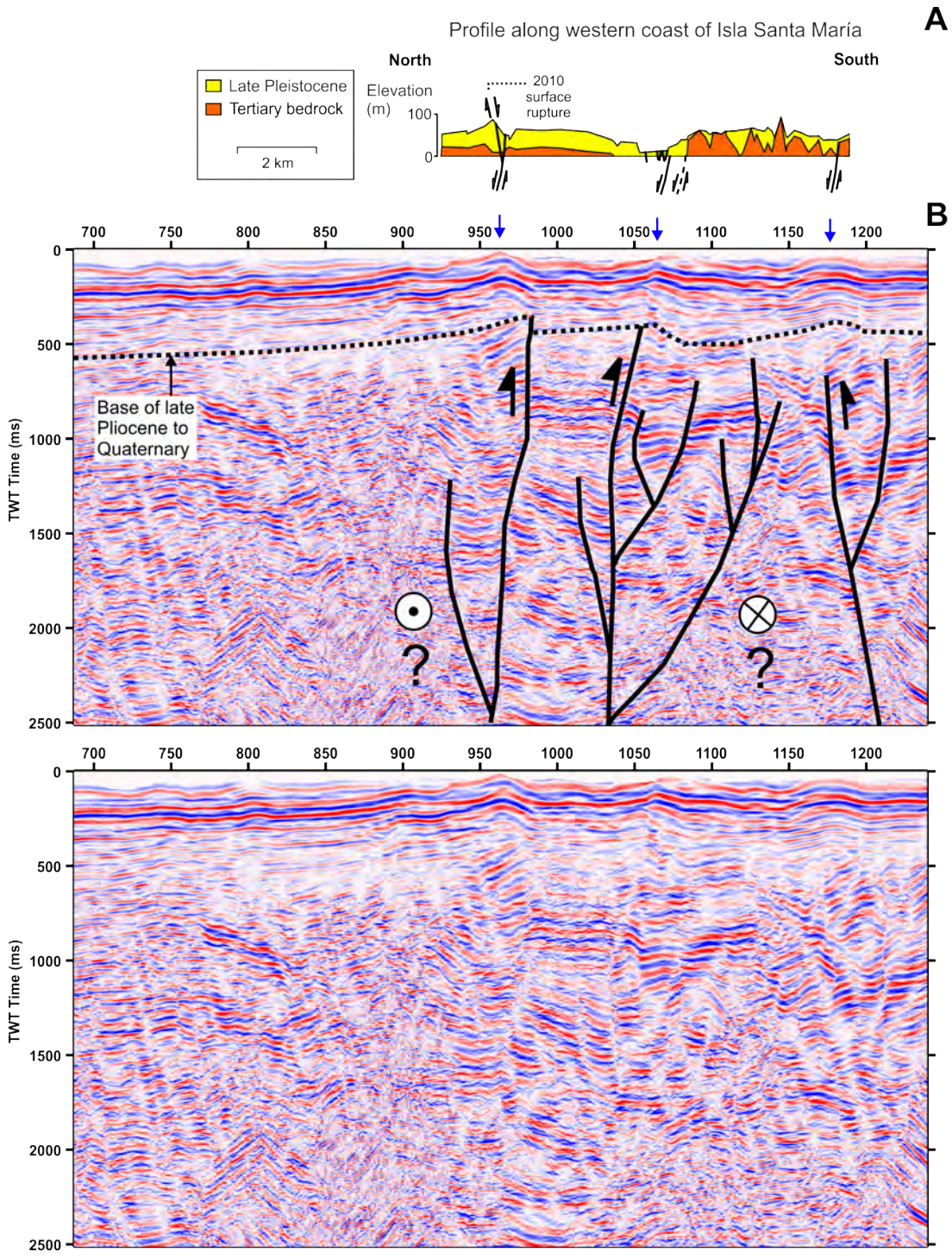

Figure DR2. Subsurface structure off ISM. A: Profile along the western coast of ISM from sea-cliff exposures showing the position of the three systems of active normal faults (Melnick et al., 2006). Note variations in paleotopography of the Tertiary bedrock and changes in thickness of the late Pleistocene unit segmented by the normal fault systems. B: Seismic reflection profile ENAP D4-13. Location indicated by thick red line in Figure DR1. Blue arrows indicate position of active reverse-fault cored anticlines, which are coincident with the location of active normal faults at ISM. Positive flower geometry suggests a component of strike-slip motion. Base of late Pliocene-Quaternary unit (Tubul Formation) from correlation of seismic profiles and boreholes in the region (Melnick et al., 2009).

Site	Longitude (deg)	Latitude (deg)	East (mm)	North (mm)	Up (mm)	East error	North error	Up error	No. pre	No. post
STMA	-73.5290	-37.0154	-4890	-428	1712	-	-	-	2	2
STDO	-73.5457	-37.0225	-4912	-392	1851	48	15	15	6	6
STCA	-73.5304	-37.0588	-5105	-381	1416	16	5	20	6	3

Table DR1. Coseismic GPS displacements at ISM. Values have been obtained from linear regression of pre and post-earthquake campaign measurements (Figure 2B). No. pre–Number of pre-earthquake measurements collected between 2004 and 2009; No. post–Number of post-earthquake measurements. Each pre-earthquake measurement session consists of at least 48 hours of continuous data acquisition, whereas post-earthquake sessions include at least 12 hours of data. See (Moreno et al., 2008; Moreno, 2010; Moreno et al., 2011) for processing details.

Interferogram	orbit	θ	α	h_a (m)	$B_\perp$ (m)
20100115 - 20100302	Ascending	39°	344°	~ 140	~ 470

Table DR2. Detail of the interferogram constructed for this study.

θ: Incidence angle.

α: Satellite heading angle, measured clockwise from north.

$B_\perp$: Perpendicular baseline.

h_a: Height ambiguity – the amount of topography needed to produce one topographic fringe.

East	North	Throw	East	North	Throw	East	North	Throw
630788.09	5905670.23	60	630798.45	5905710.04	41	630253.7	5905652.64	0
630785.9	5905645.55	15	630556.82	5905623.19	0	630245.92	5905661.09	0
630785.77	5905648.94	18	630546.01	5905624.91	0	630252.3	5905665.6	5
630786.64	5905654.8	42	630536.5	5905623.58	0	630260.68	5905674.12	5
630786.23	5905660.59	45	630486.85	5905627.14	0	630271.2	5905681.27	0
630786.7	5905664.25	65	630494.23	5905624.85	0	630269.93	5905681.37	0
630787.1	5905665.71	46	630499.58	5905623.35	0	630275.31	5905686.94	0
630789.16	5905673.69	40	630503.56	5905621.45	0	630278.41	5905689.28	0
630789.69	5905677.02	45	630498.72	5905624.94	0	630275.1	5905663.92	0
630790.29	5905680.28	82	630502.43	5905623.57	5	630281.78	5905668.56	0
630791.02	5905682.67	62	630507.43	5905621.32	0	630280.28	5905664.16	0
630791.62	5905683.67	74	630507.13	5905622.48	0	630291.04	5905671.54	0
630794.02	5905687.07	45	630513.46	5905621.7	10	630297.04	5905676.79	0
630786.23	5905661.82	47	630521.61	5905620.48	8	630299.53	5905678.62	0
630793.5	5905686.53	37	630535.47	5905622.43	0	630312.29	5905685.75	0
630795.58	5905692.13	50	630530.66	5905621.51	5	630321.4	5905692.66	0
630795.57	5905688.74	45	630187.62	5905576.79	32	630318.51	5905692.03	0
630793.97	5905695.26	54	630193.07	5905579.94	30	630326.41	5905697.85	0
630795.5	5905697.68	60	630196.11	5905583.91	25	630313.85	5905684.83	0
630797.55	5905700.38	42	630195.89	5905587.82	15	630325.41	5905693.37	0
630855.32	5905744.51	30	630198.41	5905590	10	630331.34	5905694.16	0
630862.52	5905745.14	0	630215.02	5905607.46	15	630347.05	5905709.86	0
630848.26	5905746.59	0	630218.55	5905610.6	15	630349.41	5905705.01	0
630844.7	5905743.4	0	630220.37	5905611.97	5	630340.44	5905700.18	0
630846.2	5905744.42	10	630229.91	5905630.33	8	630345.31	5905701.1	0
630843.38	5905744.38	25	630242.15	5905640.54	0	630330.21	5905692.4	0
630837.26	5905737.82	30	630233.28	5905644.14	10	630360.99	5905750.14	0
630834.77	5905735.29	42	630247.6	5905661.57	0	630365.97	5905761.53	0
630841.52	5905738.87	35	630244.53	5905643.23	6	630357.32	5905725.24	0
630801.34	5905714.18	40	630249.59	5905649.44	5	630361.89	5905731.76	0

Table DR3. Throw measurements used in Figures 3A and 3B. Coordinates in UTM 18S, throw in cm.

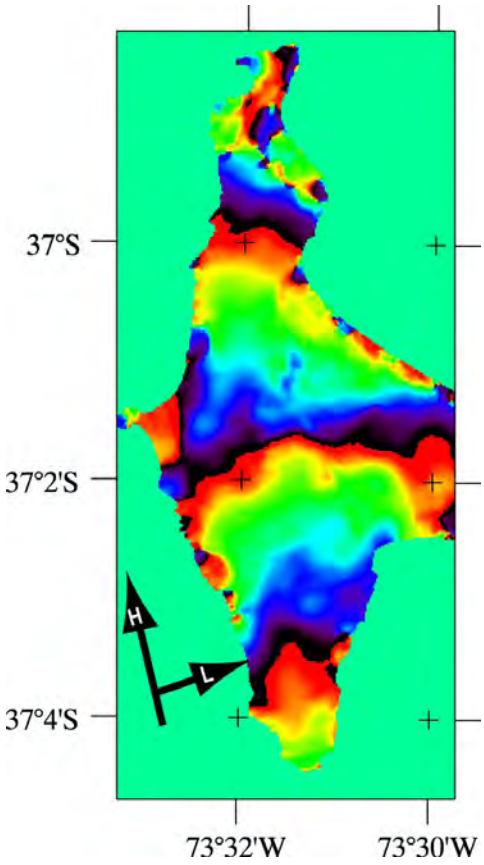

Figure DR3. Coseismic ascending ALOS interferogram used in this study. Each color cycle (fringe) in the wrapped interferogram represents ~12 cm of displacement in the satellite line-of-sight (LOS) direction. Black arrows illustrate directions of satellite track (H) and LOS vector (L).

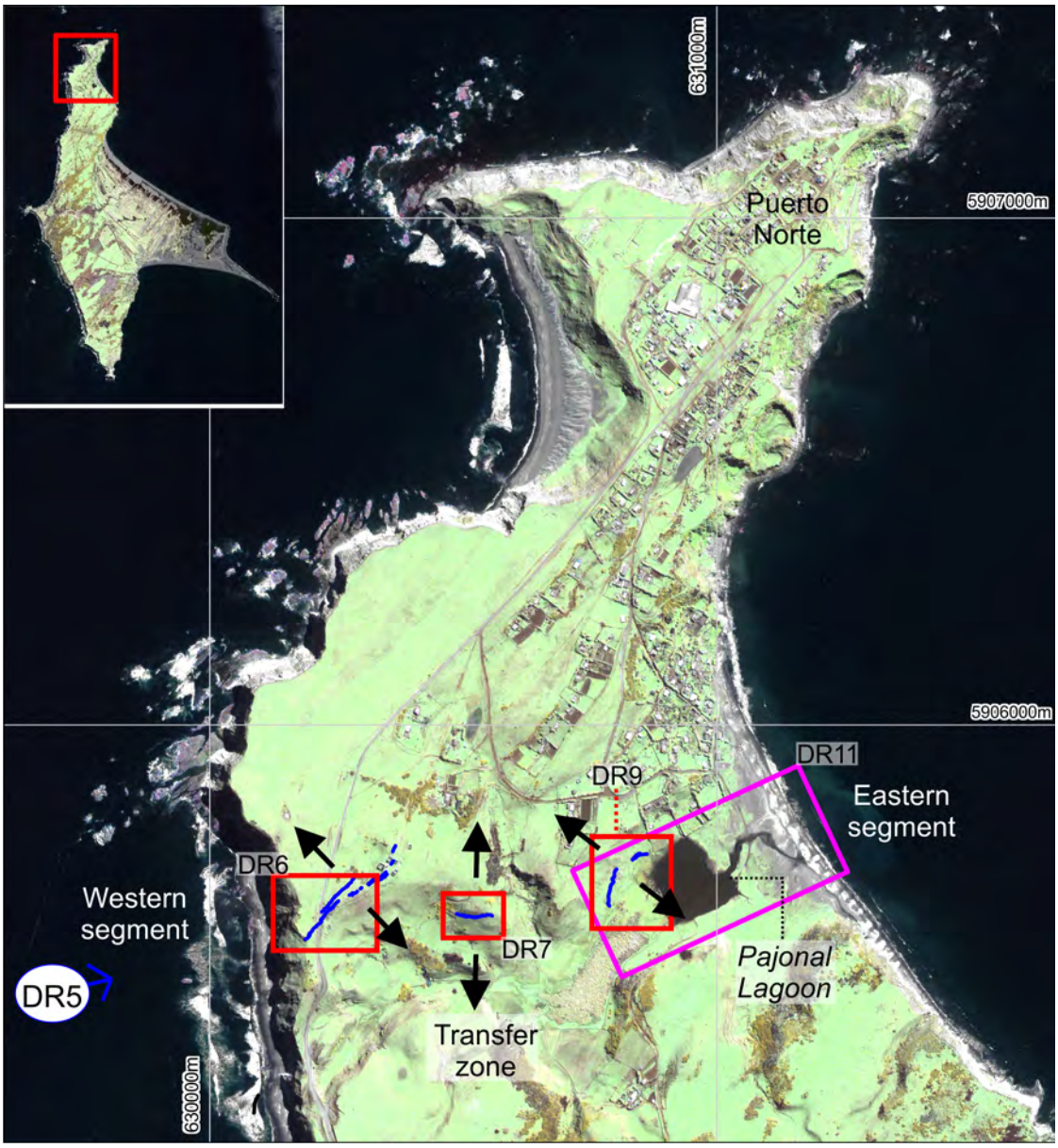

Figure DR4. Index maps of surface ruptures at ISM. Base Ikonos image collected September 18, 2007. Blue lines indicate traces of the surface breaks, black arrows show displacement direction. Letters and red boxes show location of field views and maps in the following figures. Coordinates are in UTM 18 south projection.

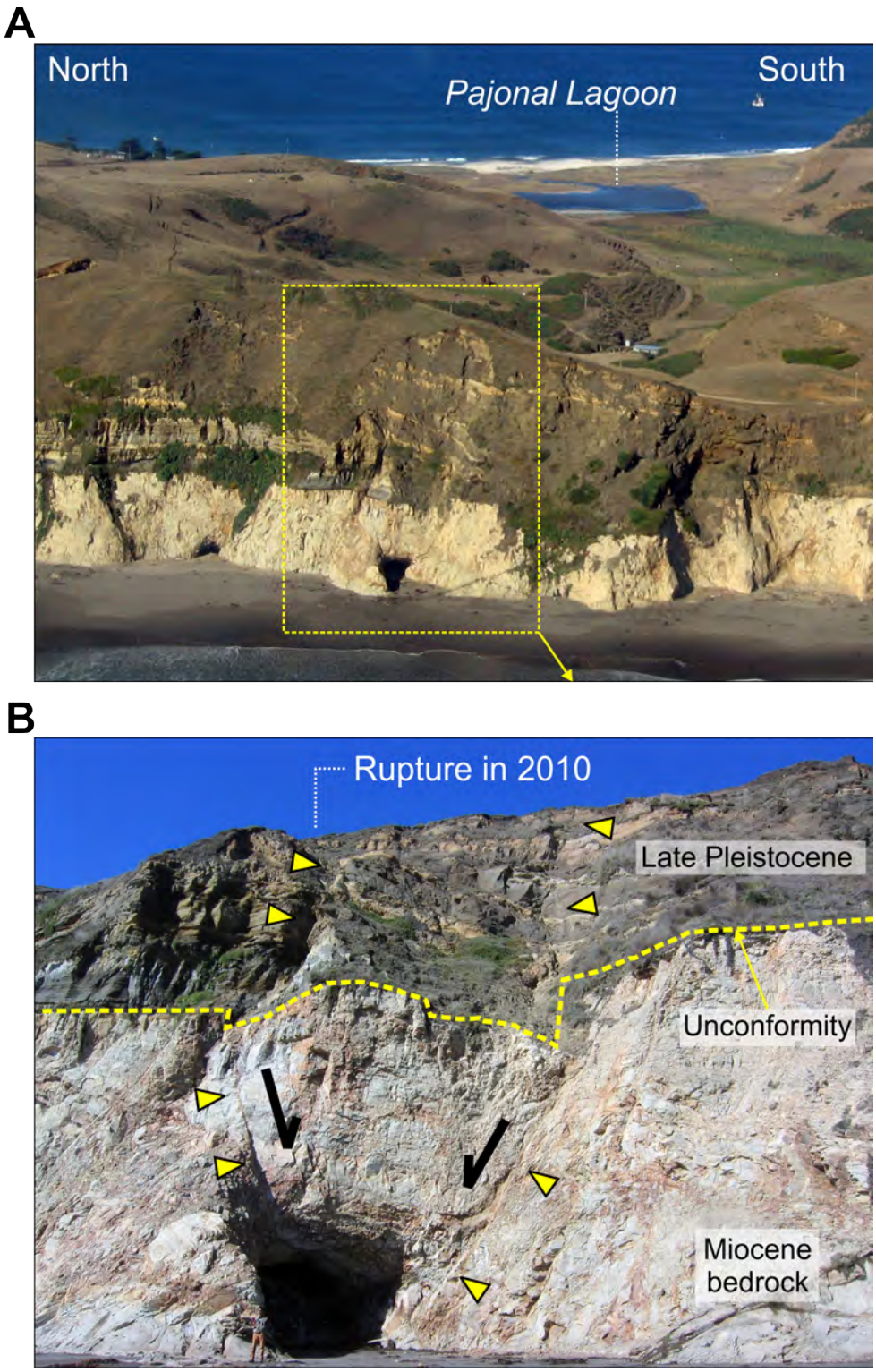

Figure DR5. Views of normal faults exposed at sea cliff. Photos taken March 2004. The exposures have been covered by landslides triggered during the 2010 earthquake. A: Aerial view towards the east showing location of sea-cliff exposures. B: Normal faults offsetting the unconformity between Miocene bedrock and late Pleistocene strata and forming an assymetric graben structure, highlighted by yellow triangles. The main fault is at the right. Person at the left entrance of the cave for scale. The sea cliff is about 60 m high.

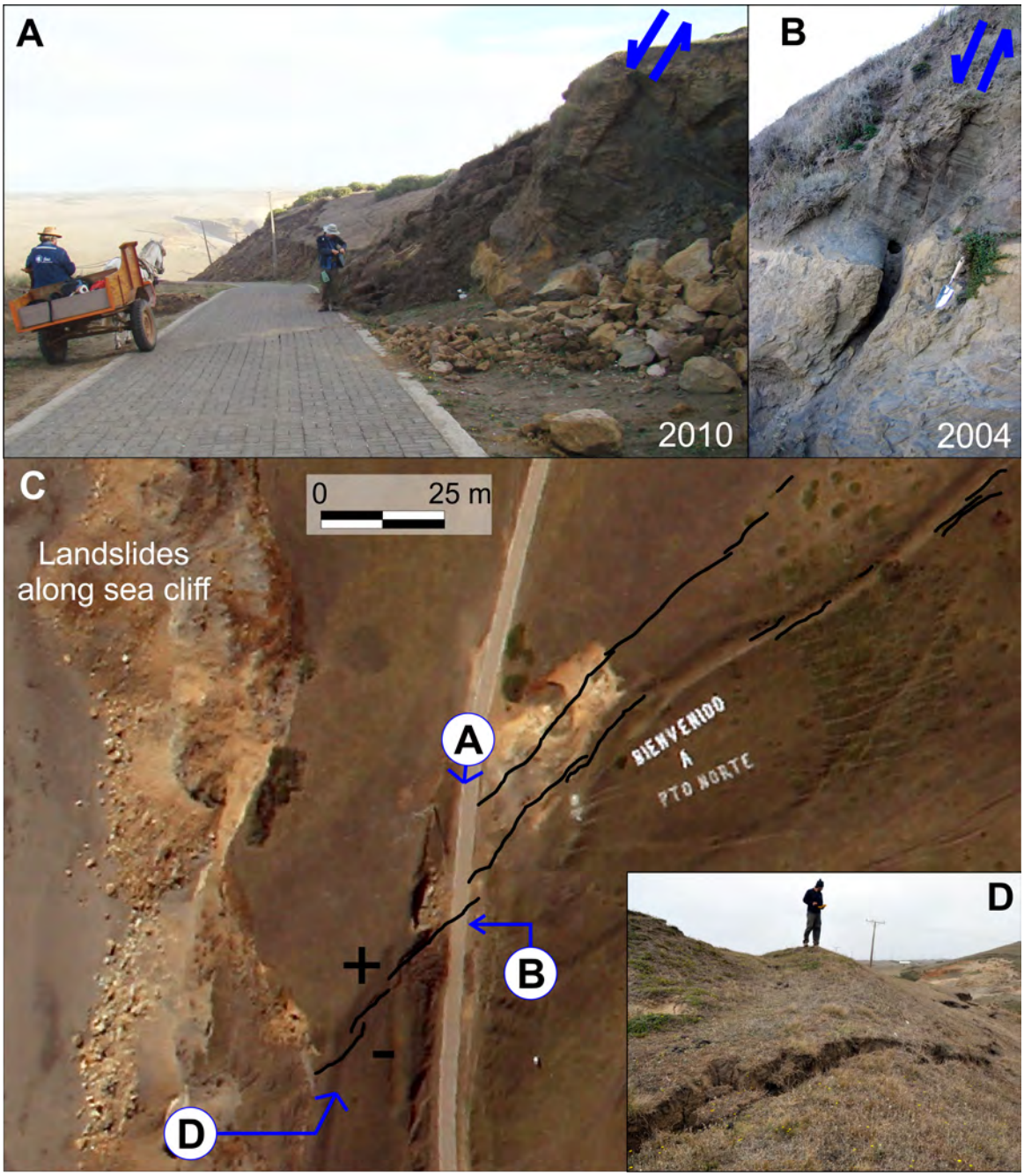

Figure DR6. Views of the western fault segment. A: Fault rupture across the paving stone with 15 cm of vertical throw and exposed on adjacent road cut; photo taken March 22, 2010. B: Same road cut photographed in March 2004, exposing a steeply-dipping fault with 15 cm of displacement, offsetting ~27-ka-old eolian strata. C: Vertical air photo (25-cm digital image from March 25, 2010) showing fault traces and location of field views. Signs indicate relative displacements. Note the presence of fresh landslides along the sea cliff, which covered fault exposures showed in Figure DR5. Note the label "Bienvenido a Pto Norte" east of the road, meaning "welcome to the town of Puerto Norte". D: Close-up view of en échelon surface ruptures at the southwestern tip of this segment. Photo taken March 12, 2010, person for scale.

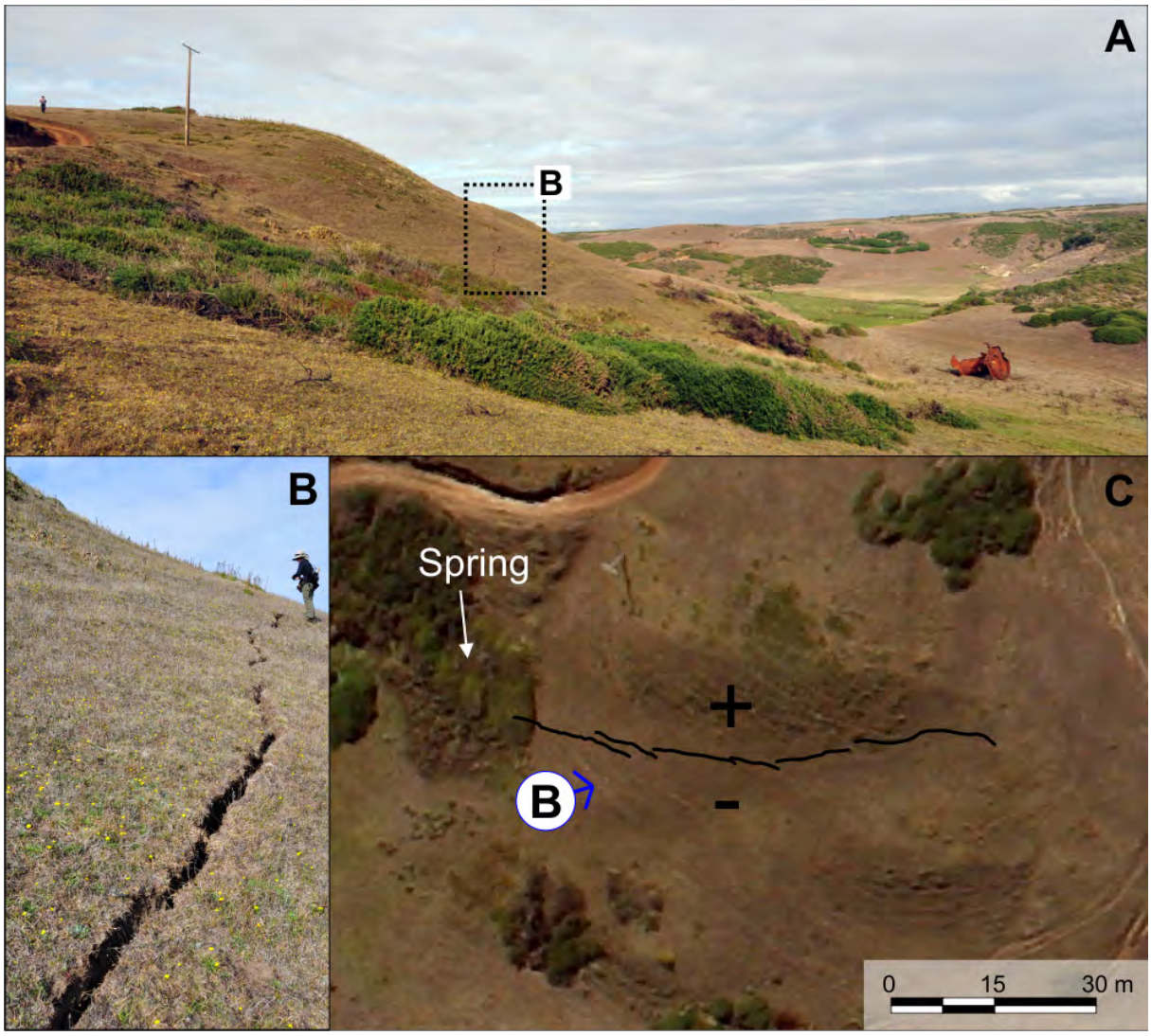

Figure DR7. Views of the transfer zone segment. A: View toward the east showing location of the rupture at mid slope on the steep valley flank. Person and electricity pole for scale. B: Detailed view of the rupture with 10 cm of opening and 5-10 of throw, person for scale. Photos collected March 22, 2010. C: Air photo (as in Figure DR6) showing fault traces, relative displacement, and location of field view. Note the left-steping en échelon pattern. The western termination of the rupture is coincident with the position of a fresh-water spring.

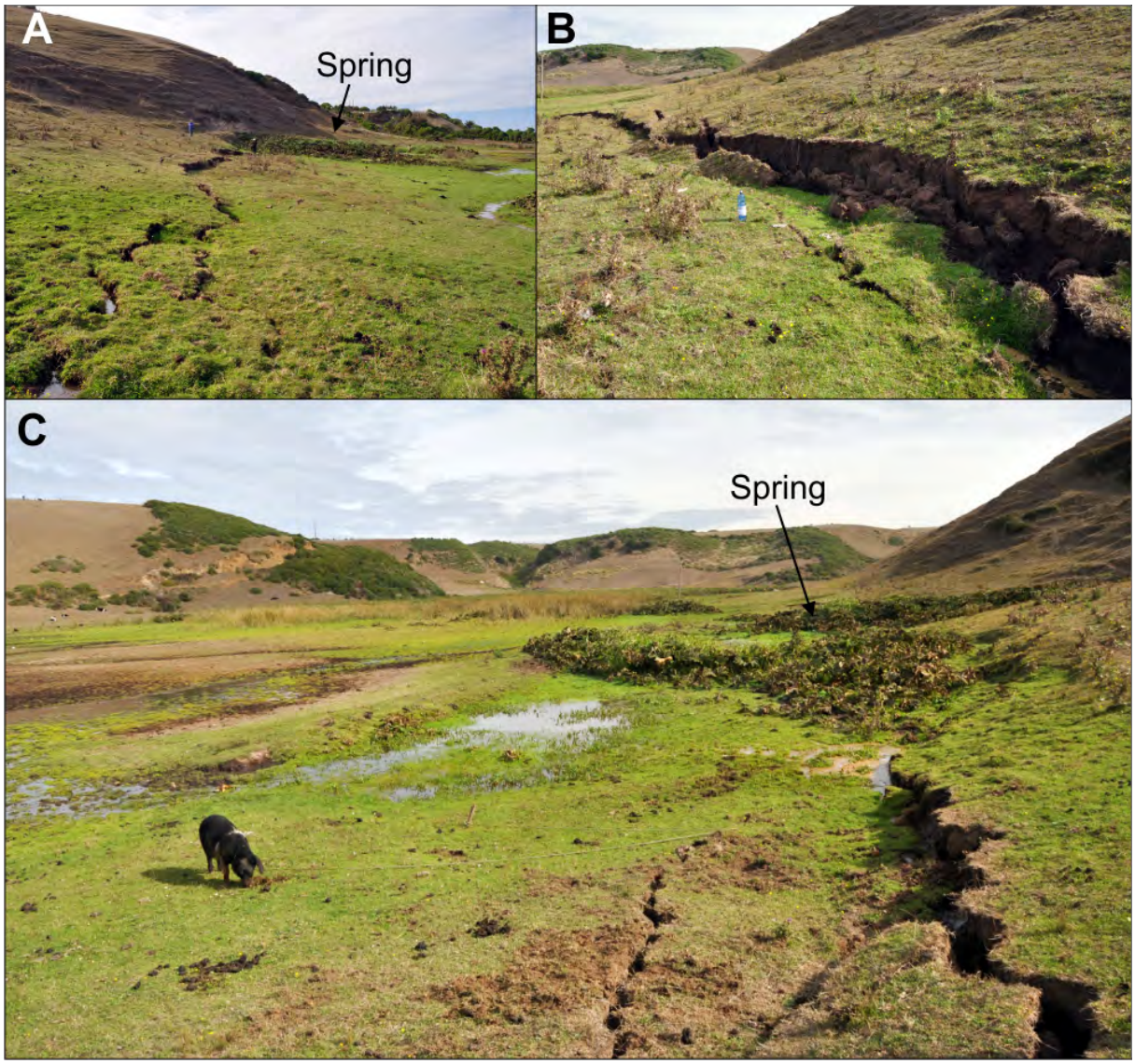

Figure DR8. Views of the eastern fault segment. A: View toward the northeast at the western fault tip. Note the increase in vertical throw toward the spring. Two persons in blue and black on the footwall (left of fault) and hanging wall blocks, respectively, as scale. B: View of the site with the maximum measured vertical throw of 82 cm, 1.5-liter water bottle for scale. C: View of continuous fluid offspring from the fault rupture, adjacent to a pig. The fault rupture becomes discontinuous when entering a zone of thick bushes associated with a long-lived spring. Inhabitants recalled continuous fluid flow bubbling out of the fault during the following 3 days after the earthquake. Fluids were still emerging from the fault during our second visit on March 22, 2010, when these photos were collected.

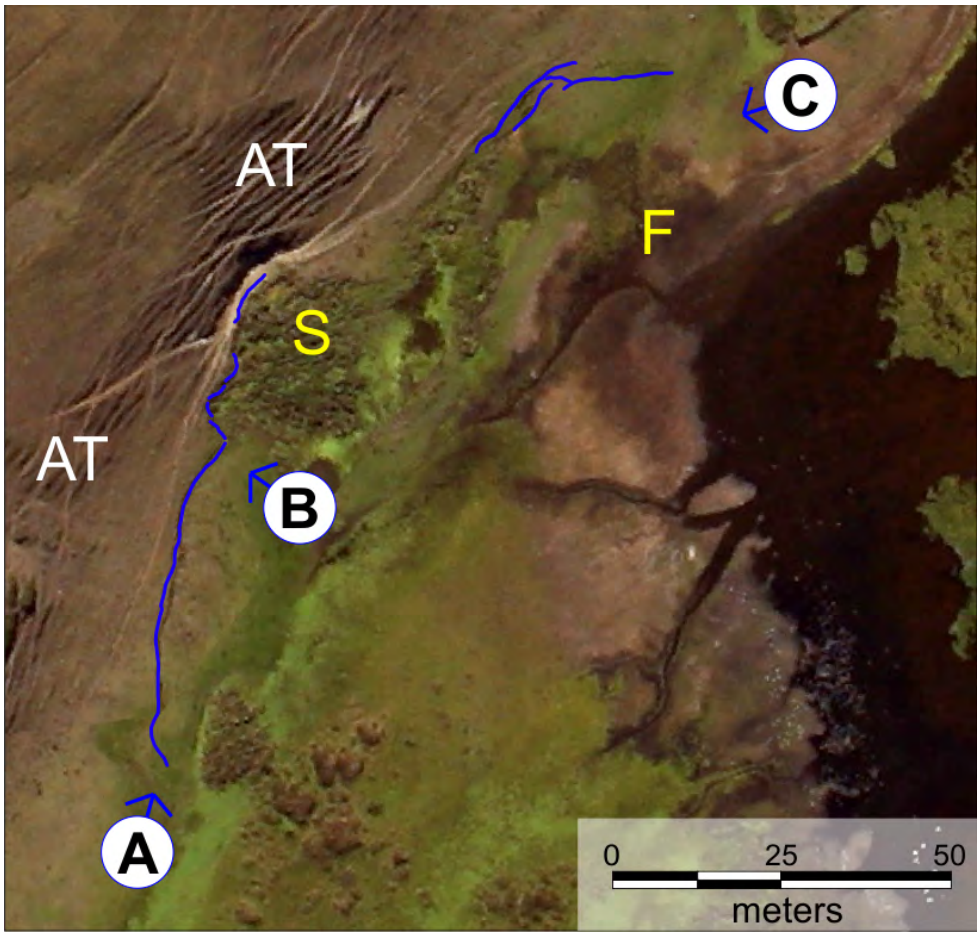

Figure DR9. Air photo collected March 25, 2010, and fault traces along the eastern rupture segment (blue lines). Capital letters in circles show location of field views in Figure DR8. The location of a spring along the fault (S) and site of continuous fluid offspring after the 2010 earthquake along surface fault break (F) are shown. The linear features west of the fault trace are animal tracks (AT) and footpaths.

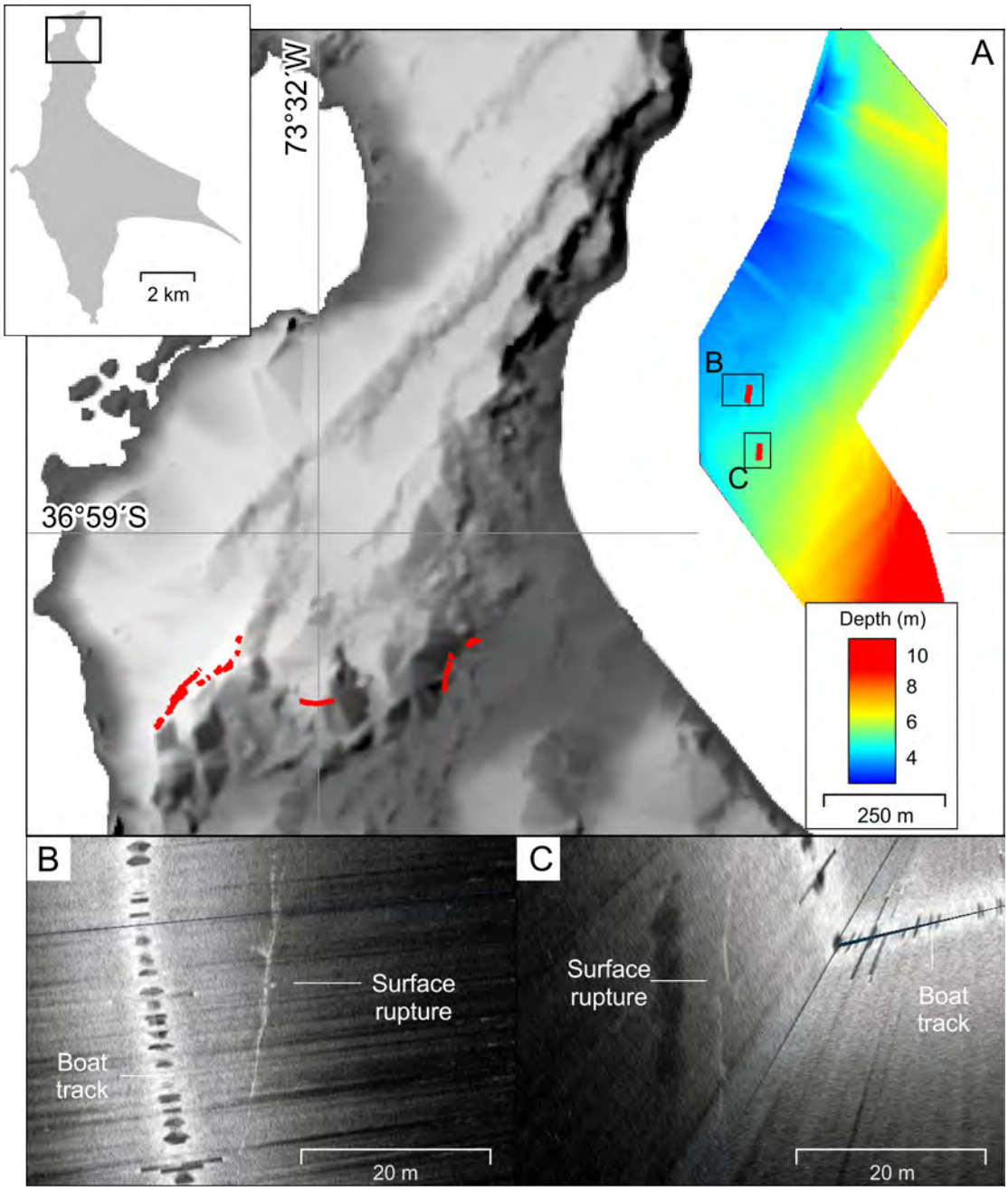

Figure DR10. Offshore surface ruptures. A: Bathymetry of the embayment northeast of ISM. Red lines show location of onshore surface fault ruptures (Figure 3A) and offshore features. B: and C: side-scan sonar images of the northern and southern features, interpreted as offshore surface fault ruptures.

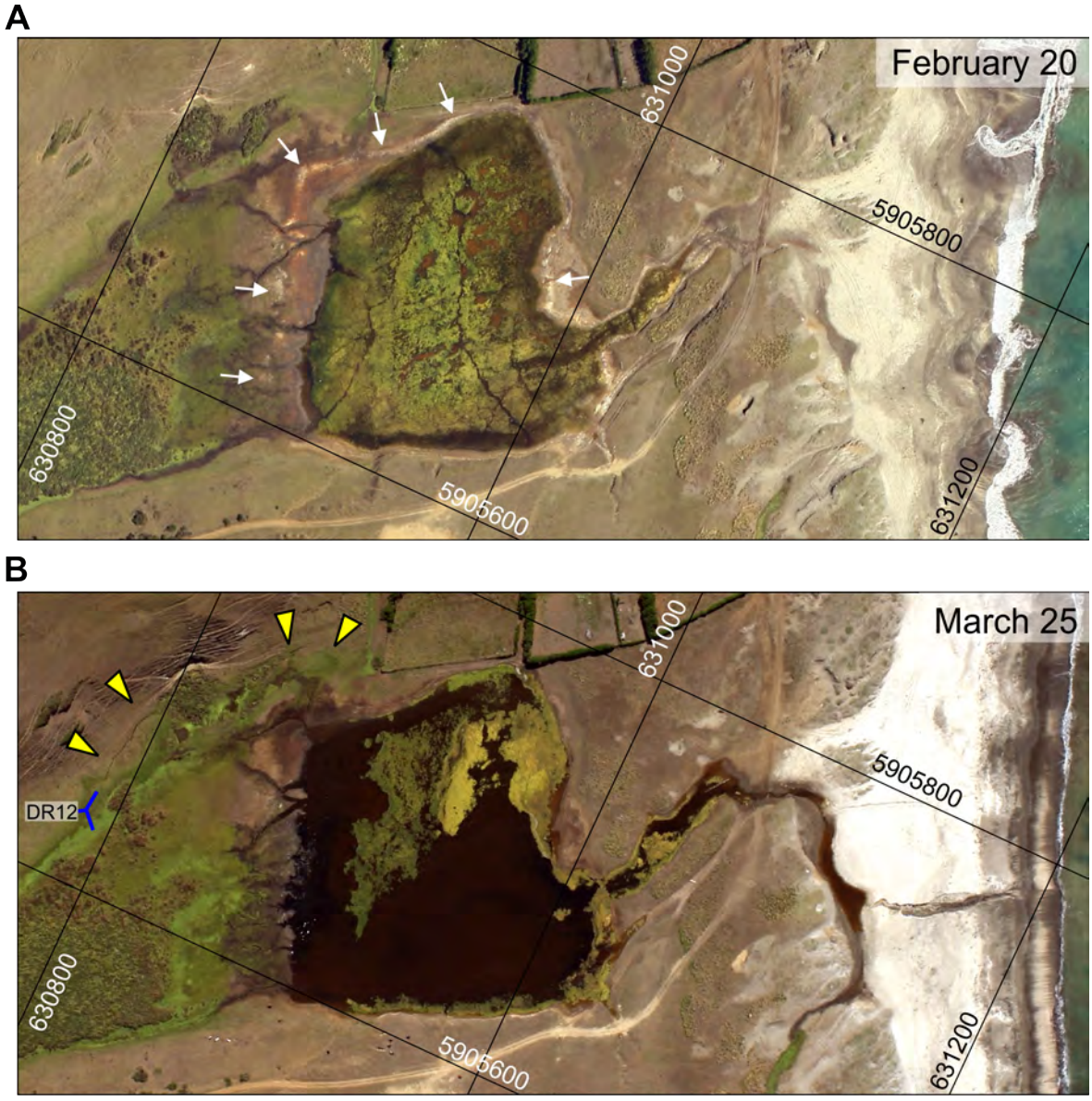

Figure DR11. Pre- and post-earthquake air photos of the Pajonal Lagoon. A: Image collected 7 days before the event (February 20, 11:17, UTC -0300). B: Image collected 25 days after the earthquake (March 25, 14:10, UTC -0300). Note the change in water level, which resulted from continuous rush of fluids along the fault break, indicated by yellow triangles. See Figure DR4 for location, Figure DR8 for a close up of the surface rupture, and Figure DR12 for a panoramic view. White arrows highlight location of the overflow shoreline, corresponding to the level reached by the lagoon after the earthquake.

Figure DR12. Panoramic view (4 merged images) towards the east. The surface rupture can be observed on the left, with water outflowing towards the Pajonal Lagoon in the background. Eucebio Loyola for scale standing on the footwall. Location of view in Figure DR11.

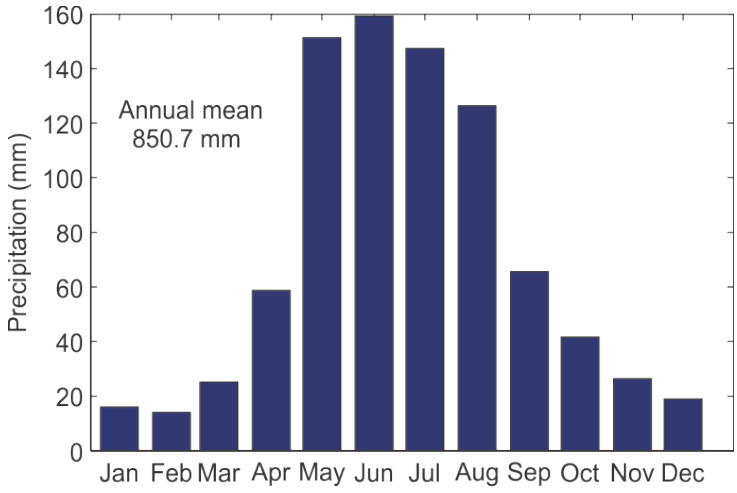

Figure DR13. Monthly precipitation at ISM (Devynck, 1970).

References

Chen, C. W., and Zebker, H. A., 2001, Two-dimensional phase unwrapping with use of statistical models for cost functions in nonlinear optimization: Journal of the Optical Society of America, v. 18, p. 338-351.

Devynck, J. L., 1970, Contribución al estudio de la circulación atmosférica en Chile y el clima de la región del Bío-Bío - Contribution to the study of atmospheric circulation in Chile and climate of the Bio-Bio region: Departement of Geophysics, University of Concepción.

Goldstein, R. M., and Werner, C. L., 1998, Radar interferogram filtering for geophysical applications: Geophysical Research Letters, v. 25, p. 4035-4038.

Melnick, D., Bookhagen, B., Echtler, H., and Strecker, M., 2006, Coastal deformation and great subduction earthquakes, Isla Santa María, Chile (37°S): Geological Society of America Bulletin, v. 118, p. 1463-1480.

Melnick, D., Bookhagen, B., Strecker, M., and Echtler, H., 2009, Segmentation of megathrust rupture zones from fore arc deformation patterns over hundreds to millions of years, Arauco peninsula, Chile: Journal of Gephysical Research, v. 114, p. B01407.

Melnick, D., Cisternas, M., Moreno, M., and Norambuena, R., 2011, Estimating coseismic coastal uplift with an intertidal mussel: calibration for the 2010 Maule, Chile earthquake (Mw=8.8): Quaternary Science Reviews.

Melnick, D., and Echtler, H. P., 2006, Inversion of forearc basins in south-central Chile caused by rapid glacial age trench fill: Geology, v. 34, p. 709-712.

Moreno, M., Melnick, D., Rosenau, M., Bolte, J., Klotz, J., Echtler, H., Baez, J. C., Bataille, K., Chen, J., Bevis, M., Hasse, H., and Oncken, O., 2011, Heterogeneous plate locking in the South-Central Chile subduction zone: building up the next great earthquake: Earth and Planetary Science Letters, v. 305, p. 413-424.

Moreno, M. S., 2010, Active deformation in the southern Andes from GPS and FEM models [PhD Thesis]: Technische Universitat Berlin, 136 p.

Moreno, M. S., Klotz, J., Melnick, D., Echtler, H., and Bataille, K., 2008, Active faulting and heterogeneous deformation across a megathrust segment boundary from GPS data, south-central Chile (36-39°S): Geochemistry, Geophysics, Geosystems, v. 9, p. Q12024.